





Magnetic incommensurability, short-range correlations, and properties of Ho₇Rh₃A. F. Gubkin ^{1,2,*} A. A. Vaulin ¹ T. Tsutaoka,^{3,†} A. F. Prekul,¹ K. P. Skokov ⁴ and N. V. Baranov ^{1,2}¹*M. N. Mikheev Institute of Metal Physics, UB RAS, 620108 Yekaterinburg, Russia*²*Institute of Natural Sciences and Mathematics, Ural Federal University, 620083 Yekaterinburg, Russia*³*Higher Education School, Hiroshima University, Higashi-Hiroshima 739-8524, Japan*⁴*Chelyabinsk State University, 454001 Chelyabinsk, Russia*

(Received 31 July 2022; revised 24 September 2022; accepted 29 September 2022; published 19 October 2022)

The crystal structure, thermal properties, and magnetic state of the rare-earth intermetallic compound Ho₇Rh₃ was studied using the measurements of the AC and DC magnetic susceptibility, magnetization, specific heat and thermal expansion, as well as by neutron and synchrotron powder diffraction. Below the Néel temperature $T_N = 32$ K, an incommensurate antiferromagnetic (AFM) structure of the spin density wave (SDW) type was observed, described by the magnetic superspace group $Cmc2_1, I'(00g)0sss$ and the propagation vector $\mathbf{k}_{IC} = (0\ 0\ 0.389)$. Further cooling leads to the spin reorientation transition and squaring-up transformation of the SDW magnetic structure below $T_{I1} = 22$ K. The spin reorientation transition is accompanied by the emergence of a ferromagnetic component in the incommensurate magnetic structure upon cooling below $T_{I2} = 9$ K. Using neutron diffraction, the existence of a short-range antiferromagnetic order was revealed up to temperatures twice as high as T_N . These short-range AFM correlations were found to affect the magnetic susceptibility and thermal expansion, while the crystal structure retains its hexagonal symmetry below and above the Néel temperature.

DOI: [10.1103/PhysRevB.106.134419](https://doi.org/10.1103/PhysRevB.106.134419)**I. INTRODUCTION**

Noncentrosymmetric compounds attract much attention in the cutting-edge research fields due to a plethora of emergent properties such as unconventional superconductivity, topological phases, nontrivial quantum properties, and other interesting behaviors related to strong spin-orbit coupling [1–3]. Among the binary rare-earth intermetallic compounds a family of R_7T_3 (R = rare-earth metal, T = Rh, Pd, Ni) compounds represents a rare example of noncentrosymmetric crystal structure of Th₇Fe₃ type (SG $P6_3mc$) [4–6]. The crystal structure of R_7T_3 compounds is built of trigonal prisms which are formed by R atoms occupying one $2b$ and two $6c$ Wyckoff sites while T atoms occupying another single $6c$ Wyckoff site are engaged inside these prisms (see Fig. 1). The linkage coefficient (LC) was introduced by Parthé *et al.* [7] as a measure of interconnection between the trigonal prisms in the R_nT_m family. It was estimated to be as low as $LC = 2$ for R -richest R_3T (T = Ni, Co) compounds and $LC = \frac{18}{7}$ for R_7T_3 family reflecting good isolation of single T atoms inside of the R -based trigonal prisms. Isolated T atoms do not bear any magnetic moment due to the filling of their $3d$ ($4d$) band by outer-shell electrons of R atoms [8]. However, long-range exchange interactions of the Ruderman-Kittel-Kasuya-Yosida (RKKY) type between localized magnetic moments of R atoms is considered to be the driving force of magnetic ordering phenomena in the R -rich R_nT_m compounds. Interplay between strong crystal electric field and competing RKKY-exchange interactions results in rich magnetic phase diagrams,

complicated magnetic structures, and enhanced short-range magnetic order frequently observed in R -rich R_nT_m compounds [9].

Despite plenty of published data on macroscopic properties of R_7T_3 compounds [10–19], not much is known about their magnetic properties on a microscopic level up to date. There are a number of neutron diffraction studies reporting complex incommensurate magnetic structures in R_7T_3 compounds in terms of propagation vectors and their temperature dependencies [12,20,21]. However, there are quite a few works reporting quantitative description of the incommensurate magnetic structures observed in Nd₇Ni₃ [22], Ce₇Ni₃ [23], Nd₇Rh₃ [24], and Nd₇Pd₃ [25]. Among them only Refs. [23–25] used the representation analysis technique to simplify refinement of magnetic structure by imposing symmetry induced restrictions on the magnetic moments of R ions residing in the three nonequivalent sites.

The magnetic structure of Ce₇Ni₃ reported by Kadowaki *et al.* [23] was found to be incommensurate with the propagation vector $\mathbf{k}_{IC} = (0\ 0\ \mu)$ just below the Néel temperature T_{N1} while further cooling below T_{N2} results in emergence of the commensurate component indexed by $\mathbf{k}_C = (0\ 0\ \frac{1}{4})$. The high temperature incommensurate magnetic structure was found to be of a spin-wave type and described by a combination of four irreducible representations (irreps): two one-dimensional irreps Δ_2 and Δ_3 describing the c -axis component of magnetic structure and two two-dimensional irreps Δ_5 and Δ_6 describing the in-plane component of magnetic structure. Both Δ_5 and Δ_6 irreps were brought to fit nonzero Bragg peaks of $(00l \pm \mu)$ type with l -even and l -odd, respectively. The second work of Rayaprol *et al.* [24] reports an incommensurate transverse spin wave (TSW) magnetic structure with a

*agubkin@imp.uran.ru

†Deceased.

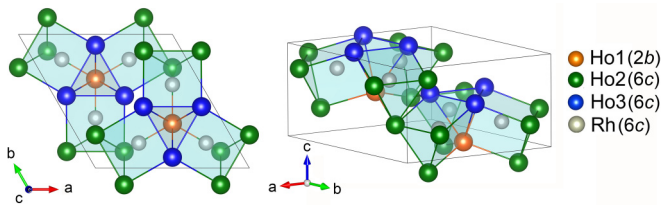


FIG. 1. Visualization of a hexagonal crystal structure of R_7T_3 compounds formed by R -based trigonal prisms encaging T atoms.

propagation vector of $\mathbf{k}_{IC} = (00\mu)$ in the Nd_7Rh_3 compound just below the Néel temperature T_{N1} . The further cooling below T_{N2} brings the sample to a mixed magnetic state where high temperature incommensurate magnetic phase coexists with commensurate magnetic phase described by a propagation vector $\mathbf{k} = 0$. Again, both two-dimensional irreps Δ_5 and Δ_6 (denoted by authors as IR3 and IR6, correspondingly) were involved in the Rietveld refinement. Finally, a neutron diffraction study of Nd_7Pd_3 , recently reported by Mudryk *et al.* [25], revealed an incommensurate TSW magnetic structure with a propagation vector $\mathbf{k}_{IC} = (00\mu)$ just below the Néel temperature T_{N1} . A further cooling down to T_C results in magnetic phase transition from an incommensurate anti-ferromagnetic (AFM) structure to a ferromagnetic structure accompanied by a change of crystal symmetry from $P6_3mc$ to $Cmc2_1$. Again, a high temperature incommensurate magnetic structure was refined using basis vectors associated with two-dimensional irreps Δ_5 and Δ_6 . A combination of these irreps were brought into the refinement of magnetic structures of Nd_7Rh_3 and Nd_7Pd_3 because of the misfit of $(000)^\pm$ satellites by a model based on a single irrep.

The magnetic superspace group approach was shown to be a powerful method of analysis of incommensurate magnetic structures particularly (i) when one deals with the irreps of dimension $N > 1$ and (ii) when two active irreps are involved in magnetic phase transition [26,27]. As far as many members of the R_7T_3 family exhibit incommensurate magnetic structures described by a combination of two-dimensional irreps, it would be interesting to consider their magnetic ordering below Néel temperature in terms of the magnetic superspace group approach. In this work we present a study of the incommensurate magnetic structure of Ho_7Rh_3 performed by a Rietveld refinement of the neutron diffraction data using the magnetic superspace group approach. We also used linear and nonlinear AC-magnetic susceptibility measurements as a source of complementary data about magnetic symmetry breaking in Ho_7Rh_3 below the Néel temperature. Linear thermal expansion as well as synchrotron diffraction were employed to check for temperature induced crystal structure phase transitions in Ho_7Rh_3 .

II. EXPERIMENTAL DETAILS

Ho_7Rh_3 ingots were prepared by arc-melting of the constituent elements of 99.9% Ho and 99.96% Rh in high purity argon atmosphere. In total, two Ho_7Rh_3 polycrystalline samples were synthesized. The x-ray diffraction attestation of Ho_7Rh_3 samples was performed using a Empyrean x-ray diffractometer (PANalytical) with $\text{Cu-K}\alpha$ radiation

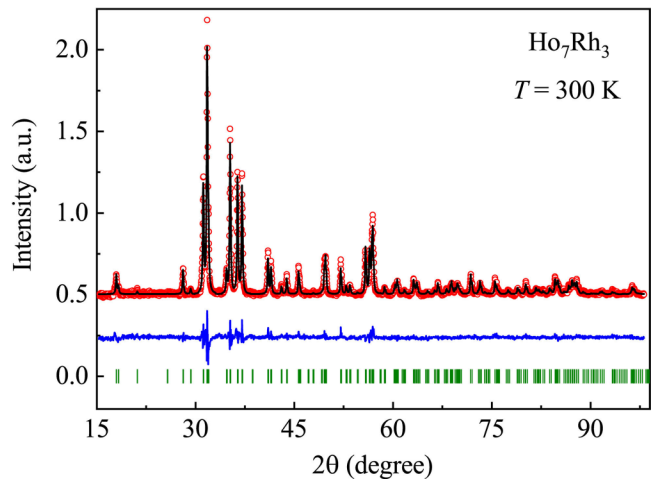


FIG. 2. Rietveld refinement of the x-ray diffraction data measured on the first sample. Observed (red circles), calculated (black line), and difference (blue line) x-ray diffraction patterns for the first Ho_7Rh_3 sample measured at room temperature.

($\lambda = 1.54056 \text{ \AA}$) at room temperature. It has been found that the first Ho_7Rh_3 sample is single phase while the second sample contains a trace amount of impurity phases $\text{Ho}_5\text{Rh}_3 \sim 2 \text{ wt.}\%$ and $\text{Ho}_2\text{O}_3 \sim 4 \text{ wt.}\%$. The crystal structure of both samples was found to be in good agreement with the model (space group $P6_3mc$) previously reported for other compounds of the $R_7\text{Rh}_3$ series (see Fig. 2) [5,12]. The first sample was used for heat capacity, magnetic measurements, and synchrotron diffraction, while the neutron diffraction measurements were performed on the second sample.

The linear AC and DC magnetic susceptibility data were measured using MPMS-XL and PPMS instruments (Quantum Design, USA). The standard PPMS sweep mode was used for temperature control with a temperature change rate of 1 K min^{-1} . Measurements of the AC magnetic susceptibility were carried out using driven field amplitude $H_a = 2 \text{ Oe}$ and frequencies $f = 0.777, 7.77, 77.7, \text{ and } 777 \text{ Hz}$. Time dependent magnetization of a system $M(t)$ in response to an external oscillating magnetic field $H_{ac} = H_a \cos \omega t$ can be expressed as follows:

$$M(t) = M_{1\omega} \sin(\omega t + \theta_{1\omega}) + M_{2\omega} \sin(2\omega t + \theta_{2\omega}) + M_{3\omega} \sin(3\omega t + \theta_{3\omega}) + \dots, \quad (1)$$

where $w = 2\pi f$, $M_{n\omega} = H_a \chi_{n\omega}$ is the n th harmonic components for integer $n = 1, 2, 3, \dots$, and $\theta_{n\omega}$ is the delay in phase of each component against the ideal response signal, which is $\pi/2$ out of phase with the driving field signal. $M_{1\omega}$ component represents the linear term of the AC susceptibility. Emergence of the higher harmonics $M_{n\omega}$ ($n = 2, 3, 4, \dots$) in the AC susceptibility data reflects distortion of the ideal sinusoidal $M(t)$ signal due to the nonlinear terms $\chi^{(m)}$ ($m = 1, 2, 3, \dots$) in expansion of the magnetization M with general magnetic field H [28]:

$$M(H) = \chi^{(0)}H + \chi^{(1)}H^2 + \chi^{(2)}H^3 + \dots. \quad (2)$$

Even harmonics $M_{n\omega}$ ($n = 2, 4, \dots$) arise when the time-inversion symmetry is broken and considered to be a

hallmark of a spontaneous magnetization. Odd harmonics $M_{n\omega}$ ($n = 3, 5, \dots$) are connected with the breaking of a spatial symmetry due to the magnetic phase transition to the long-range ordered magnetic state (accompanying the large phase change) or spin-glass-like freezing (not accompanying the large phase change) [28–32]. AC magnetic susceptibility reported in this work is shown as a combination of real and imaginary components $\chi_{n\omega} = M_{n\omega}/H_a = \chi'_{n\omega} + i\chi''_{n\omega}$ ($n = 1, 2, 3$).

The heat capacity measurements were performed in the temperature range 2–300 K in zero field using a PPMS instrument (Quantum Design, USA). Thermal expansion studies were carried out on the polycrystalline Ho_7Rh_3 sample having $l = 1.64$ mm length between the parallel faces using the capacitive mini-dilatometer option for PPMS by Kuechler Innovative Measurement Technology [33].

Neutron diffraction experiments with wavelength $\lambda = 1.826$ Å were carried out using the neutron diffractometer for high efficiency, high resolution measurements (HERMES) installed at JRR-3M in JAERI at Tokai, Japan. For the refinement of magnetic structure, we used the JANA2006 program [34]. The ISODISTORT program which is a part of ISOTROPY software suite was used for the symmetry analysis of magnetic structures in Ho_7Rh_3 [35]. Magnetic point, space, and superspace groups reported in this paper are given in accordance with the recently published unified magnetic space groups symbols [36]. The synchrotron XRD measurements were carried out on a high-resolution powder diffraction beamline ID22 at the European Synchrotron Radiation Facility (ESRF, France). X-ray diffraction patterns were measured with $\lambda = 0.354205(4)$ Å on the powder sample packed in the 0.3 mm capillary. Data were recorded in a wide temperature range of 4–300 K using a liquid helium cooled cryostat.

III. RESULTS AND DISCUSSION

A. DC magnetic susceptibility and heat capacity

Magnetic susceptibility curves of Ho_7Rh_3 measured using zero field cooling $\chi^{\text{ZFC}}(T)$ and field cooling $\chi^{\text{FC}}(T)$ procedures in applied magnetic fields $H = 0.1, 0.5,$ and 1 kOe as well as heat capacity curve $C_p(T)$ are shown in Fig. 3. As one can see from Fig. 3, magnetic phase transition on cooling from paramagnetic to antiferromagnetic state can be observed as a barely visible cusp on the $\chi(T)$ and λ -type anomaly on the $C_p(T)$ curves at $T_N \approx 32$ K. Steplike jumps of the DC magnetic susceptibility can be observed at $T_{i1} \approx 22$ K and $T_{i2} \approx 9$ K for all measured magnetic susceptibility curves on cooling below the Néel temperature. These anomalies were previously reported by Tsutaoka *et al.* [12,14,37] from magnetic measurements on the single crystal samples and ascribed to the temperature induced spin-reorientation transitions. A thermomagnetic hysteresis of $\chi^{\text{ZFC}}(T)$ and $\chi^{\text{FC}}(T)$ curves measured in an applied field of 100 Oe can be observed in the low temperature range $T < 22$ K [see Fig. 3(a)] while no visible hysteresis can be seen in the temperature range $T_1 < T < T_N$. Slight increase of the external magnetic field above 500 Oe suppresses the observed irreversibility of $\chi^{\text{ZFC}}(T)$ and $\chi^{\text{FC}}(T)$ curves.

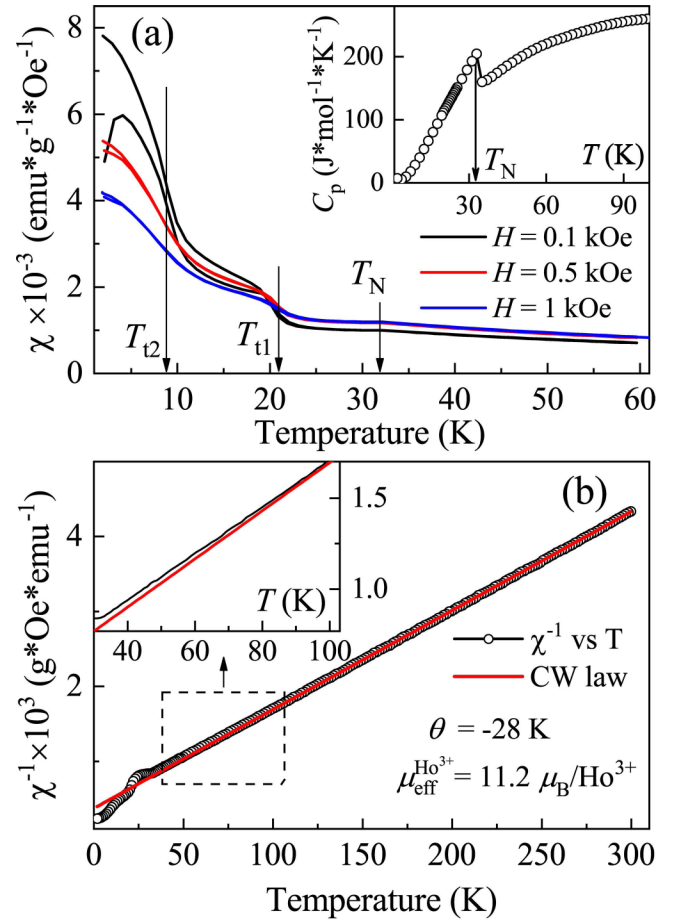


FIG. 3. Temperature dependence of the DC magnetic susceptibility measured at various applied fields as ZFC and FC procedures. (b) Curie-Weiss law fit of the inverse susceptibility measured at $H = 1$ kOe.

The inverse susceptibility χ^{-1} measured at $H = 1$ kOe as a function of temperature T is plotted in Fig. 3(b). The high temperature part of the inverse susceptibility curve ($T > 150$ K) has been fitted using the Curie-Weiss (CW) law. However, we noticed that the χ^{-1} versus T dependence begins to deviate upward from the CW line when the temperature decreases below 100 K, i.e., far to reach critical temperature. This deviation may indicate the presence of short-range magnetic correlations above T_N . Bearing in mind the large Ho^{3+} effective magnetic moment, a temperature-independent contribution to the inverse susceptibility from the core diamagnetism and Van-Vleck paramagnetism is not taken into account. The effective magnetic moment (μ_{eff}) is estimated to be $\mu_{\text{eff}}^{\text{Ho}^{3+}} = 11.2 \mu_B$. This is slightly larger than the theoretical value $10.58 \mu_B$ for a free Ho^{3+} ion. However, this value is in good agreement with the one reported by Tsutaoka *et al.* [14]. Both short-range magnetic correlations above the Néel temperature and spin fluctuations in the d -electron subsystem may affect the high temperature susceptibility behavior above the Néel temperature. Negative paramagnetic Curie temperature $\theta_p = -28$ K implies dominance of the antiferromagnetic exchange interactions of the RKKY type.

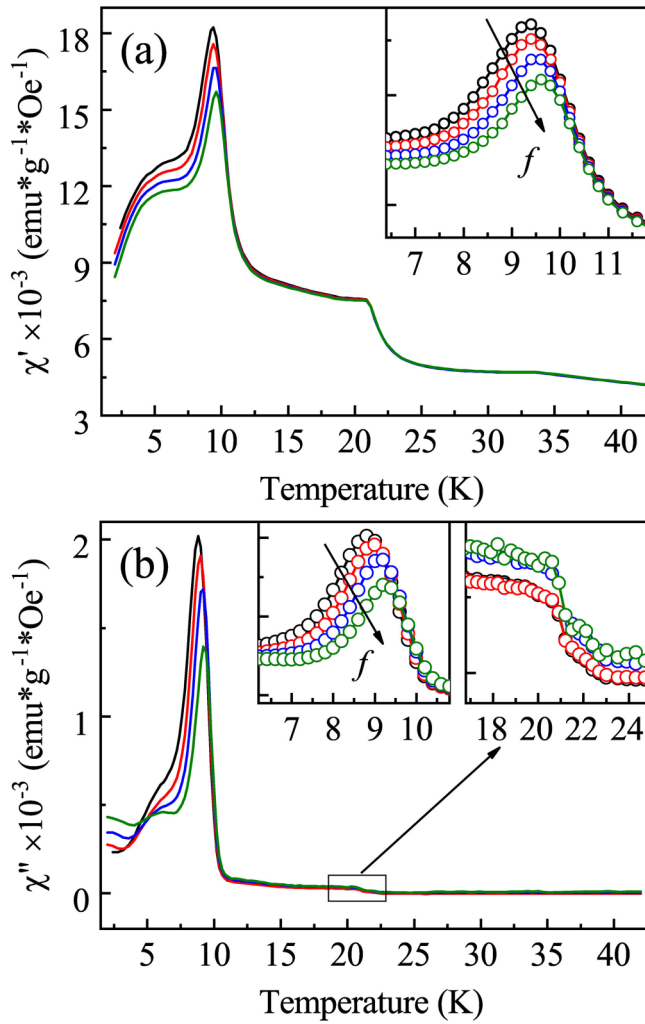


FIG. 4. Temperature dependencies of the (a) real $\chi'(T)$ and (b) imaginary $\chi''(T)$ components of the AC susceptibility measured at $H_a = 2$ Oe and $f = 0.77, 7.77, 77.7,$ and 777 Hz. Enlarged cusps at $T_{12} \approx 9$ K are shown in the insets. Arrows mark direction from the low frequency to the high frequency.

B. AC magnetic susceptibility in Ho_7Rh_3

1. Linear AC magnetic susceptibility

The real $\chi'(T)$ and imaginary $\chi''(T)$ components of the AC susceptibility are plotted as a function of temperature in Fig. 4. The real component $\chi'(T)$ is reminiscent of the DC magnetic susceptibility curve and exhibits a barely visible hump at the Néel temperature $T_N \approx 32$ K, a steplike jump at $T_{11} \approx 22$ K, and a glasslike anomaly at $T_{12} \approx 9$ K overlapping with a low temperature shoulder. No substantial dispersion $\chi'(\omega)$ or absorption $\chi''(\omega)$ can be observed in the temperature range $T_{12} < T < T_N$. However, pronounced frequency dependence of both $\chi'(T)$ and $\chi''(T)$ susceptibility curves develops on cooling below T_{12} . The imaginary component $\chi''(T)$ has no visible anomaly around the Néel temperature, as it is expected for ordinary antiferromagnets, and exhibits a small jump at T_{11} . Similar to the real component $\chi'(T)$, the imaginary component $\chi''(T)$ shows a sharp cusp around T_{12} temperature followed by a low-temperature shoulder. It can

be seen that both amplitude and position of the observed cusps depend on the driven field frequency. For instance, their position shifts towards higher temperatures when increasing the driven field frequency, as it is usually observed in spin glasses [38]. The amplitude of the cusp on the $\chi'(T)$ curve reduces its value when increasing the driven field frequency in agreement with typical spin-glass behavior. However, contrary to what is usually observed in spin glasses, the cusp on the $\chi''(T)$ curve substantially reduces its height when increasing the frequency. As it was shown by Mydosh [39], the temperature of the cusp in the $\chi''(T)$ curve corresponds to the inflection point on the high temperature side of the $\chi'(T)$ maximum. It can be seen from the insets in Fig. 4 that this is not true in Ho_7Rh_3 .

A phenomenological classification of the glasslike systems can be done by estimation of the frequency dependence of the cusp temperature T_f described by a Mydosh parameter $\delta T_f = \frac{\Delta T_f}{T_f \Delta[\lg(f)]}$ [39]. This parameter provides a criterion to distinguish spin glass freezing from a relaxation process of noninteracting or interacting magnetic entities (magnetic clusters, superparamagnetic particles, etc). The Mydosh parameter for Ho_7Rh_3 was estimated to be $\delta T_f \approx 0.015$ by maximum at the $\chi''(T)$ curve. The estimated δT_f is among the highest reported for canonical spin glasses (0.005–0.018) [39], very close to the values observed in the rare-earth intermetallics exhibiting low temperature cluster-glass magnetic state [40] and substantially less than the ones observed for weakly interacting magnetic entities exhibiting high sensitivity to the frequency change ($\delta T_f > 0.1$) [41]. However, magnetic moments freezing and blocking effects are not the only possible mechanisms explaining glasslike anomalies on the AC susceptibility data. For instance, glasslike effects on the AC susceptibility data were previously reported to originate from changes in the domain structure and domain walls coercivity in ferrimagnetic FeCr_2S_4 [42] and in ferromagnetic $\text{Ho}_2\text{Fe}_{17}$ [43].

An effect of external DC magnetic field on the real $\chi'(T)$ and imaginary $\chi''(T)$ components of AC susceptibility is shown in Figs. 5(a) and 5(b). It can be seen that a magnetic field of 500 Oe completely suppresses the jumplike anomaly around T_{11} and spin-glass-like cusp around T_{12} . The detailed field dependence of $\chi'(T)$ and $\chi''(T)$ components measured at $T = 9$ K implies that the glasslike effects in Ho_7Rh_3 can be completely suppressed by as low a magnetic field as $H_{\text{DC}} \approx 200$ Oe (see the insets in Fig. 5).

2. Nonlinear AC magnetic susceptibility

Real $\chi'_{n\omega}$ ($n = 2, 3$) and imaginary $\chi''_{3\omega}(T)$ components of AC susceptibility measured at different frequencies $f = 77, 777,$ and 7777 Hz are shown in Figs. 6(a), 6(b) and 6(d) as a function of temperature. No sign of anomaly on the $\chi'_{2\omega}(T)$ curves can be seen at the Néel temperature $T_N = 32$ K in agreement with what one may expect for a magnetic phase transition from a paramagnetic to an antiferromagnetic state. However, all $\chi'_{2\omega}(T)$ curves reveal a barely visible anomaly around $T_{11} \approx 22$ K followed by a strong positive cusp at $T_{12} \approx 9$ K manifesting the time-reversal symmetry breaking due to the emergence of a spontaneous magnetization [28,32]. Although $\chi'_{2\omega}(T)$ is known to diverge to a negative side at T_C for a ferromagnets [44], the shape of the peak was reported

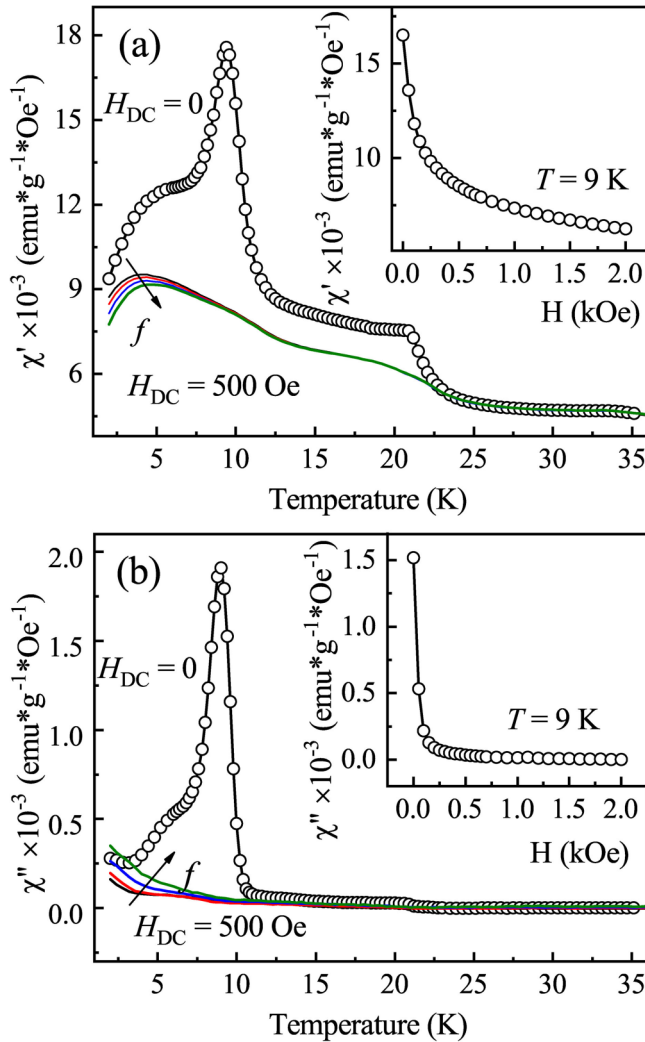


FIG. 5. Temperature dependencies of the (a) real $\chi'(T)$ and (b) imaginary $\chi''(T)$ components of the AC susceptibility measured at $H_a = 2$ Oe and $f = 0.77, 7.77, 77.7,$ and 777 Hz in applied DC magnetic field $H_{DC} = 500$ Oe. Solid line through the circles represents $\chi'(T)$ and $\chi''(T)$ curves measured at $H_{DC} = 0$. Field dependence of the real and imaginary components of AC susceptibility measured at $T = 9$ K are shown in the insets. Arrows mark direction from the low frequency to the high frequency.

to evolve dramatically from positive to negative values depending on the interplay between temperature and weak bias DC magnetic field [45]. Thus, the particular shape of the cusp observed at $T_{l2} = 9$ K could be affected by a weak remnant DC magnetic field of a 9 T superconducting magnet of our PPMS instrument.

The third harmonic curves $\chi'_{3\omega}(T)$ and $\chi''_{3\omega}(T)$ curves exhibit well resolved double-peak anomaly with a high temperature cusp at 8.5 K and a low temperature shoulder around $T \approx 6$ K [see Figs. 6(b) and 6(d)]. It can be seen that slowing of dynamics in Ho_7Rh_3 indicated by a peak in the $\chi''_{1\omega}(T)$ curve (see Fig. 4) is accompanied by a nonlinearity in magnetic response to an oscillating field $H(t)$. It has been shown theoretically that nonlinear term $\chi'_{3\omega}(T)$ diverges to the negative side at the freezing temperature T_g for spin glasses [30], exhibits divergence to the positive side below T_N for antifer-

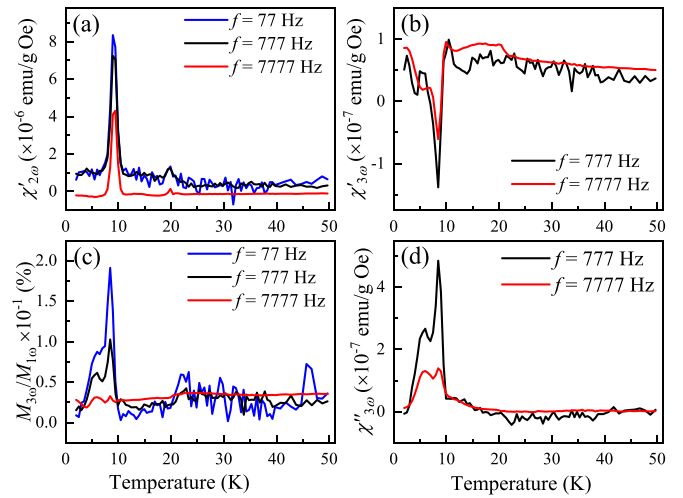


FIG. 6. Temperature dependencies of the (a) and (b) real $\chi'_{n\omega}$ ($n = 2, 3$) and (d) imaginary $\chi''_{n\omega}(T)$ components of AC susceptibility measured using driving field amplitude $H_a = 2$ Oe and $f = 77, 777,$ and 7777 Hz. (c) Temperature dependence of the Klirr factor $K = M_{3\omega}/M_{1\omega}$ plotted for $f = 77, 777,$ and 7777 Hz.

romagnets [30,46], or changes sign at T_C and diverges on both sides of T_C for ferromagnets [30,44]. However, a multidomain structure in real ferromagnets was reported to result in a purely negative peak or purely positive peaks on the $\chi'_{3\omega}(T)$ curve depending on the driving field amplitude and frequency [31,46]. The amplitude of the the cusp on the $\chi''_{3\omega}(T)$ curve is substantially higher than the one at the real component curve $\chi'_{3\omega}(T)$. This can be attributed to activation of a domain walls movement below $T_{l2} = 9$ K as it was previously reported in pure ferromagnetic Ni [31].

The Klirr factor determined as a ratio $K = M_{3\omega}/M_{1\omega}$ can be used as a measure of nonlinearity in magnetic response to the oscillating magnetic field [47]. The temperature dependence of the Klirr factor is shown in Fig. 6(c). It can be seen that magnetic response of the Ho_7Rh_3 turns out to be nonlinear below 10 K. The Klirr factor exhibits high value $K = 0.2\%$ at the low frequency of the driving field and decreases its value when increasing the frequency. Thus nonlinearity in magnetic response of Ho_7Rh_3 to the oscillating field develops in the low frequency range while in the high frequency range the response tends to be linear. Bearing in mind consistent behavior of the linear component $\chi'_{1\omega}(T)$, second and third harmonic components $\chi'_{n\omega}(T)$ and $\chi''_{n\omega}(T)$ ($n = 2, 3$) as well as the enhanced amplitude of $\chi'_{3\omega}(T)$ one can suggest that the magnetic domain walls movement is triggered by a magnetic phase transition to a ferro- or ferrimagnetic state at $T_{l2} = 9$ K.

C. Neutron diffraction of Ho_7Rh_3

1. Neutron diffraction in a paramagnetic state

Neutron diffraction pattern (NDP) of the Ho_7Rh_3 powder sample was measured in a paramagnetic state at $T = 70$ and 50 K in order to examine the crystal structure and phase purity [see Figs. 7(a) and 7(b)]. It can be seen that a broad diffuse maximum develops in the low angles region on cooling the sample in a paramagnetic state from 70 to 50 K. This

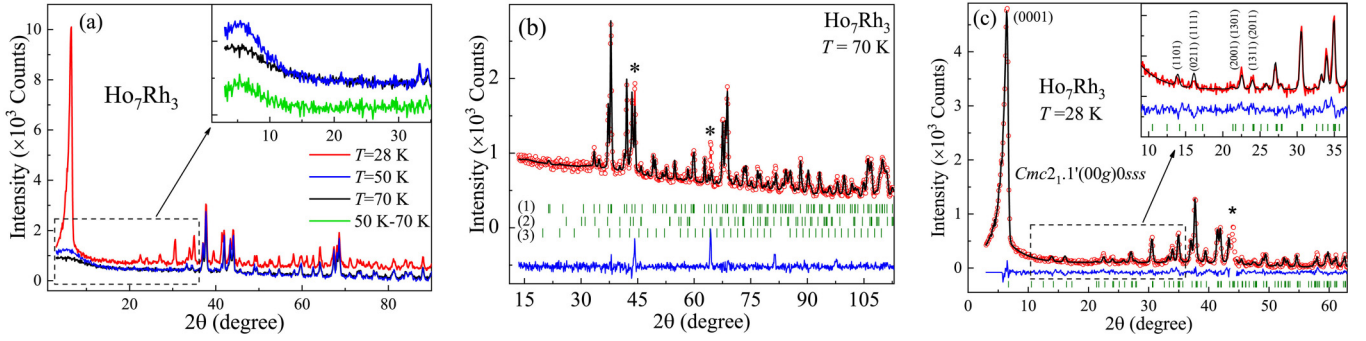


FIG. 7. (a) Neutron powder diffraction patterns for Ho_7Rh_3 measured at $T = 70, 50,$ and 28 K. The best fit result of the NDP measured (b) in a paramagnetic state at $T = 70$ K and just below the Néel temperature at $T = 28$ K. The red symbols represent the experimental profile and the solid black line represents the result of the fit. The rows of vertical marks below the patterns refer to the Bragg peaks positions: (1) main Ho_7Rh_3 phase, (2) Ho_5Rh_3 , and (3) Ho_2O_3 impurity phases. The difference between calculated and observed intensities is shown at the bottom. The asterisks (*) indicate the Bragg peaks from the sample environment.

maximum supports the suggestion that short-range antiferromagnetic order persists in Ho_7Rh_3 in a wide temperature range above the Néel temperature $T_N < T < 2T_N$. The Rietveld refinement of the crystal structure of Ho_7Rh_3 was performed using a model of the hexagonal structure with the space group $P6_3mc$, as it was reported in Ref. [5]. It was found that besides the main Ho_7Rh_3 phase a trace amount of $\text{Ho}_5\text{Rh}_3 \sim 2$ wt.% and $\text{Ho}_2\text{O}_3 \sim 4$ wt.% impurity phases exist in the sample. Two additional Bragg peaks observed at $2\theta = 64.3^\circ$ and 44.3° could not be fitted either by Ho_7Rh_3 phase or by impurity phases and were associated with the sample environment. We cut these peaks from the neutron diffraction patterns measured below the Néel temperature in order to refine a model of magnetic structure. The best fit of the neutron diffraction pattern measured at $T = 70$ K by a combination of these phases is shown in Fig. 7(b) while the refined parameters of the crystal structure of Ho_7Rh_3 are shown in Table I.

2. Magnetic structure just below the Néel temperature at $T = 28$ K

The neutron diffraction pattern of Ho_7Rh_3 was measured in a magnetically ordered state at $T = 28$ K just below the Néel temperature in order to refine a high temperature incommensurate magnetic structure having a propagation vector $\mathbf{k}_{\text{IC}} = (0\ 0\ 0.389)$ [12]. As can be seen from Fig. 7(a), a series of magnetic Bragg peaks emerged on the neutron diffraction pattern on cooling below the Néel temperature. The Le Bail fit of the neutron diffraction pattern within the angle range of

TABLE I. Atomic coordinates and the unit cell parameters obtained by the Rietveld refinement of the neutron diffraction pattern in a paramagnetic state at $T = 70$ K.

Atoms	x	y	z
Ho1(2b)	0.3333	0.6666	0.0148(3)
Ho2(6c)	0.8755(4)	0.1244(4)	0.3173(2)
Ho3(6c)	0.5412(5)	0.4592(5)	0.0198(2)
Rh(6c)	0.1877(5)	0.8122(5)	0.2493(2)
$a = 9.6904(7)$ Å, $c = 6.0877(5)$ Å			
$R_B = 6.21\%$, $R_F = 4.25\%$			

$5.6^\circ < 2\theta < 63^\circ$ revealed that the propagation vector with an adjustable $\mu = 0.389$ component is able to index all the magnetic satellites. This propagation vector corresponds to the Δ line of the Brillouin zone in accordance with the international notation after A. P. Cracknell, B. Davies, S. C. Miller, and W. F. Love (CDML) [48].

The use of the magnetic superspace groups (MSSG) approach for description of incommensurate magnetic structures suggests introduction of the modulation functions of magnetic moments defined in the $(3 + 1)$ -dimensional superspace [26,27]. The modulation function of magnetic moments \mathbf{M}_i describes the magnetic moment of an atom i with atomic coordinates \mathbf{r}_i in the unit cell shifted by a lattice translation \mathbf{T} from the zeroth unit cell and can be represented as a Fourier series:

$$\mathbf{M}_i(x_4) = \mathbf{M}_{i,0} + \sum_{n=1}^N [\mathbf{M}_{i,n}^{\sin} \sin(2\pi n x_4) + \mathbf{M}_{i,n}^{\cos} \cos(2\pi n x_4)], \quad (3)$$

where n is the number of terms in Fourier series, $x_4 = \mathbf{k}(\mathbf{T} + \mathbf{r}_i)$ is an internal coordinate, and absolute term $\mathbf{M}_{i,0} = 0$ since there is no ferromagnetic component at $T = 28$ K. The magnetic moment modulation functions $\mathbf{M}_i(x_4)$ and $\mathbf{M}_j(x_4)$ of two symmetry-related atoms i and j are constrained by the symmetry operations of the magnetic superspace group in a four-dimensional space $\{\mathbf{R}, \theta|\mathbf{t}, \tau\}$ by the following equation for purely incommensurate propagation vector [26]:

$$\mathbf{M}_j(R_I x_4 + \tau_0) = \theta \det(\mathbf{R}) \mathbf{R} \mathbf{M}_i(x_4), \quad (4)$$

where $\tau_0 = \tau + \mathbf{k}\mathbf{T}$, R_I equals +1 for \mathbf{R} keeping \mathbf{k} invariant or -1 for the one transforming \mathbf{k} to $-\mathbf{k}$, and θ is a time-reversal operation that could be +1 or -1 for a particular symmetry operator of the magnetic superspace group.

The gray magnetic space group describing the paramagnetic state of Ho_7Rh_3 is labeled as $P6_3mc.1'$ in accordance with the recently published unified magnetic space groups symbols [36]. All the symmetry operations of the polar point gray group $6mm.1'$ leave the propagation vector $\mathbf{k}_{\text{IC}} = (0\ 0\ 0.389)$ invariant. Thus the little group $G_{\mathbf{k}}$ coincides with the point gray paramagnetic group and contains all its symmetry operations. The propagation vector star $\{\mathbf{k}\}$

TABLE II. Two magnetic irreps of the gray magnetic group $P6_3mc.1'$ based on the two-dimensional irreps of the little group $6mm.1'$, OPDs in magnetic irrep space, corresponding MSSGs, and external-space part of the basis relative to the parent cell as obtained by JANA2006, corresponding MSSGs in the standard setting, and 4D supercell basis relative to the parent cell. Two isotropy subgroups of index $i = 2$ for the $Cmc2_1.1'(00g)0sss$ group are shown at the bottom (see the text). The origin of the supercell is located at $(0, 0, 0, 0)$ for all the listed groups.

Irreps	OPD	MSSG as obtained by JANA2006	MSSG in standard setting
$m\Delta_5$	$(a, 0, b, 0)$	$P6_3.1'(00g)ts$ $(\mathbf{a}_1, \mathbf{a}_2, \mathbf{a}_3)$	$P6_3.1'(00g)hs$ (No. 173.1.24.2.m130.2) $(\mathbf{a}_1, -\mathbf{a}_1 - \mathbf{a}_2, -\mathbf{a}_3 + \mathbf{a}_4, -\mathbf{a}_4)$
	(a, a, b, b)	$Cmc2_1.1'(00g)000s$ $(-\mathbf{a}_2, -2\mathbf{a}_1 - \mathbf{a}_2, -\mathbf{a}_3)$	$Cmc2_1.1'(00g)000s$ (No. 36.1.13.1.m173.2) $(\mathbf{a}_2, -2\mathbf{a}_1 - \mathbf{a}_2, \mathbf{a}_3, \mathbf{a}_4)$
	$(a, -a, b, -b)$	$Cmc2_1.1'(00g)s0s$ $(-\mathbf{a}_2, -2\mathbf{a}_1 - \mathbf{a}_2, -\mathbf{a}_3)$	$Cmc2_1.1'(00g)s0ss$ (No. 36.1.13.2.m173.2) $(\mathbf{a}_2, -2\mathbf{a}_1 - \mathbf{a}_2, \mathbf{a}_3 + \mathbf{a}_4, \mathbf{a}_4)$
	(a, b, c, d)	$P2_1.1'(0b0)0s$ $(\mathbf{a}_1, -\mathbf{a}_3, \mathbf{a}_2)$	$P2_1.1'(0b0)0s$ (No. 4.1.5.2.m8.2) $(\mathbf{a}_1, \mathbf{a}_2, \mathbf{a}_3, \mathbf{a}_4)$
$m\Delta_6$	$(a, 0, b, 0)$	$P6_3.1'(00g) - hs$ $(\mathbf{a}_1, \mathbf{a}_2, \mathbf{a}_3)$	$P6_3.1'(00g)hs$ (No. 173.1.24.2.m130.2) $(\mathbf{a}_1, \mathbf{a}_2, \mathbf{a}_3, \mathbf{a}_4)$
	(a, a, b, b)	$Cmc2_1.1'(00g)0sss$ $(-\mathbf{a}_2, -2\mathbf{a}_1 - \mathbf{a}_2, -\mathbf{a}_3)$	$Cmc2_1.1'(00g)000s$ (No. 36.1.13.1.m173.2) $(\mathbf{a}_2, -2\mathbf{a}_1 - \mathbf{a}_2, \mathbf{a}_3 + \mathbf{a}_4, \mathbf{a}_4)$
	$(a, -a, b, -b)$	$Cmc2_1.1'(00g)s0ss$ $(-\mathbf{a}_2, -2\mathbf{a}_1 - \mathbf{a}_2, -\mathbf{a}_3)$	$Cmc2_1.1'(00g)s0ss$ (No. 36.1.13.2.m173.2) $(\mathbf{a}_2, -2\mathbf{a}_1 - \mathbf{a}_2, \mathbf{a}_3, \mathbf{a}_4)$
	(a, b, c, d)	$P2_1.1'(0b0)ss$ $(\mathbf{a}_1, -\mathbf{a}_3, \mathbf{a}_2)$	$P2_1.1'(0b0)0s$ (No. 4.1.5.2.m8.2) $(\mathbf{a}_1, \mathbf{a}_2, \mathbf{a}_3 + \mathbf{a}_4, \mathbf{a}_4)$
$m\Delta_6 + m\Gamma_6$	$(a, a, b, b c, -1.732c)$	$Cmc'2_1'(00g)000$ $(-\mathbf{a}_2, -2\mathbf{a}_1 - \mathbf{a}_2, -\mathbf{a}_3)$	$Cmc'2_1'(0, 0, g)000$ (No. 36.1.13.1.m175.1) $(\mathbf{a}_2, -2\mathbf{a}_1 - \mathbf{a}_2, \mathbf{a}_3, \mathbf{a}_4)$
	$(a, a, b, b c, 0.577c)$	$Cm'c2_1'(0, 0, g)ss0$ $(-\mathbf{a}_2, -2\mathbf{a}_1 - \mathbf{a}_2, -\mathbf{a}_3)$	$Cm'c2_1'(0, 0, g)s0s$ (No. 36.1.13.2.m174.1) $(\mathbf{a}_2, -2\mathbf{a}_1 - \mathbf{a}_2, \mathbf{a}_3 + \mathbf{a}_4, \mathbf{a}_4)$

has the single arm in this case. Four one-dimensional irreducible representations (irreps) $m\Delta_1$, $m\Delta_2$, $m\Delta_3$, $m\Delta_4$ and two two-dimensional irreps $m\Delta_5$ and $m\Delta_6$ were obtained by JANA2006 [34]. As it has been shown in Ref. [26], there is direct one-to-one correspondence between the irreducible representation and the magnetic superspace group in the case of one-dimensional irreps. However, a number of different magnetic superspace groups (kernel and epikernels [27]) can be associated with a multidimensional irrep depending on the particular direction of the order parameter (OPD) vector in the representation space. Both $m\Delta_5$ and $m\Delta_6$ irreps, particular OPDs, corresponding MSSGs, and external-space part of the basis relative to the parent cell as obtained by JANA2006 are shown in Table II. Besides the fact that the Rietveld refinement was performed for magnetic space groups in the setting used in JANA2006, this representation is convenient for comparison of extinction laws for magnetic superspace groups related to $m\Delta_5$ and $m\Delta_6$ because their orthorhombic (hexagonal, monoclinic) groups are given in the same 3D basis. However, standard setting and full 4D superspace basis are necessary to avoid ambiguity and understand the difference between obtained magnetic superspace groups. We used ISODISTORT [35] and FINDSSG [49] tools in order to present these MSSGs in the standard setting providing information about full 4D superspace lattice basis and MSSG numerical identifier in accordance with Ref. [50] (see Table II).

Both two-dimensional irreps $m\Delta_5$ and $m\Delta_6$ were suggested to describe the magnetic structure just below the Néel temperature because their basis functions were found to create intensity of the zero satellite peak $(000)^\pm$ in the low angles range. A quick analysis of the extinction laws for magnetic superspace groups associated with both $m\Delta_5$ and $m\Delta_6$ was performed using the MAGNEXT tool at the Bilbao

crystallographic server [51,52]. It was found that symmetry operation $\{2_z|00\frac{1}{2}0\}$ contained in all magnetic superspace groups of the $m\Delta_5$ irrep provides a systematic absence for $(00lm)$ Bragg peaks having $l = 2n$. Contrary, a symmetry operation $\{2_z|00\frac{1}{2}\frac{1}{2}\}$ contained in all magnetic superspace groups of the $m\Delta_6$ irrep (shown in bold in Table III) gives rise to a systematic absence for $(00lm)$ Bragg peaks having $l = 2n + 1$. Thus, the only two-dimensional irrep contributing to an experimentally observed magnetic zero satellite of $(000m)$ type (where $m = \pm 1$) should be $m\Delta_6$ while no contribution is expected for any model of magnetic structure associated with $m\Delta_5$. In this work we applied only $m\Delta_6$ irrep in order to refine the magnetic structure of Ho_7Rh_3 . The symmetry operations of the MSSGs $P6_3.1'(00g)hs$, $Cmc2_1.1'(00g)0sss$, and $Cmc2_1.1'(00g)s0ss$, i.e., epikernels of the $m\Delta_6$ irrep, are shown in Table III in accordance with the format accepted in JANA2006.

The Rietveld refinement has been performed for all three models associated with the $m\Delta_6$ irrep using a magnetic superspace group setting used in JANA2006. The phase of the modulation for every tested magnetic superspace group is not fixed by symmetry because there are no symmetry operations transforming \mathbf{k} to $-\mathbf{k}$. Thus, it has been manually fixed by forcing one of the refined components to be zero. The best fit quality was found for $Cmc2_1.1'(00g)0sss$ group which describes TSW magnetic modulation propagating over all Ho sites along the c axis of the parent hexagonal structure. It should be noted that the fit quality obtained for $P6_3.1'(00g)hs$ model is good as well and it can be further improved if we allow a slight elliptical modulation for TSW waves propagating over Ho2 and Ho3 sites. However, a proper model seems to be $Cmc2_1.1'(00g)0sss$ group because it has two magnetic subgroups of index 2 which are compatible with

TABLE III. Symmetry operations of the magnetic superspace group $P6_3.1'(00g)hs$, $Cmc2_1.1'(00g)0sss$, and $Cmc2_1.1'(00g)s0ss$ described by corresponding symmetry cards as used in the program JANA2006. A complete set of symmetry operations can be obtained from the presented ones by combining them with the operation $\{1'|0, 0, 0, \frac{1}{2}\}$.

$P6_3.1'(00g)hs$ Origin at (0,0,0,0)	$Cmc2_1.1'(00g)0sss$ Origin at (0,0,0,0)	$Cmc2_1.1'(00g)s0ss$ Origin at (0,0,0,0)
x_1, x_2, x_3, x_4, m	x_1, x_2, x_3, x_4, m	x_1, x_2, x_3, x_4, m
$-x_2, x_1 - x_2, x_3, x_4 + \frac{1}{3}, m$	$-x_1, x_2, x_3, x_4, m$	$-x_1, x_2, x_3, x_4 + \frac{1}{2}, m$
$-x_1 + x_2, -x_1, x_3, x_4 + \frac{2}{3}, m$	$x_1, -x_2, x_3 + \frac{1}{2}, x_4 + \frac{1}{2}, m$	$x_1, -x_2, x_3 + \frac{1}{2}, x_4, m$
$-x_1, -x_2, x_3 + \frac{1}{2}, x_4 + \frac{1}{2}, m$	$-x_1, -x_2, x_3 + \frac{1}{2}, x_4 + \frac{1}{2}, m$	$-x_1, -x_2, x_3 + \frac{1}{2}, x_4 + \frac{1}{2}, m$
$x_2, -x_1 + x_2, x_3 + \frac{1}{2}, x_4 + \frac{5}{6}, m$	$x_1, x_2, x_3, x_4 + \frac{1}{2}, -m$	$x_1, x_2, x_3, x_4 + \frac{1}{2}, -m$
$x_1 - x_2, x_1, x_3 + \frac{1}{2}, x_4 + \frac{1}{6}, m$		
$x_1, x_2, x_3, x_4 + \frac{1}{2}, -m$		

the in-plane weak ferromagnetism (see the Discussion section). The refined magnetic parameters as well as agreement factors obtained for MSSG $Cmc2_1.1'(00g)0sss$ are shown in Table IV. The best fit result of the neutron diffraction pattern measured at $T = 28$ K by MSSG $Cmc2_1.1'(00g)0sss$ is shown in Fig. 7(c). The schematic visualizations of magnetic structure described by MSSG $Cmc2_1.1'(00g)0sss$ and two other considered groups $P6_3.1'(00g)hs$ and $Cmc2_1.1'(00g)s0ss$ are shown in Fig. 8.

3. Low temperature magnetic structure

The neutron diffraction pattern measured at $T = 4.5$ K was found to keep its incommensurate magnetic Bragg peaks described by the propagation vector $\mathbf{k}_{IC} = (00\mu)$ with $\mu = 0.388$ as can be seen in Fig. 9. Additional magnetic satellites indexed by a third harmonic $3\mathbf{k}_{IC}$ were observed by a single crystal neutron diffraction below 20 K in Ref. [12] and were confirmed on the neutron powder diffraction data $T = 4.5$ K in this work. Emergence of the contribution from odd harmonic implies evolution of the spin-density wave towards magnetic structure with equal moments via the squaring-up process. A further cooling across the $T_{I2} = 9$ K results in emergence of a spontaneous magnetization which manifests itself as a brief anomaly of the DC and AC susceptibility $T_{I2} = 9$ K. Emergence of the in-plane spontaneous magnetization suggests loss of the time-inversion symmetry which is evidenced by a peak in the $\chi'_{2\omega}(T)$ curve. Thus the symmetry operation $\{1'|000\frac{1}{2}\}$ must be dropped from the magnetic superspace group $Cmc2_1.1'(00g)0sss$ describing a high temperature magnetic structure.

TABLE IV. Refined components of the incommensurate magnetic moment modulation functions M_i^{\sin} and M_i^{\cos} obtained for symmetrically nonequivalent magnetic atoms Ho1, Ho21, Ho22, Ho31, and Ho32 using magnetic superspace group $Cmc2_1.1'(00g)0sss$. Amplitude of the TSW propagating over the corresponding Ho site is shown in the last column.

Site	M_x^{\sin}	M_y^{\sin}	M_z^{\sin}	M_x^{\cos}	M_y^{\cos}	M_z^{\cos}	$ M _{\max}$
Ho1	0.9(8)	0	0	6.2(4)	0	0	6.3(4)
Ho21	1.9(2)	1.8(2)	0 ^a	3.9(3)	3.8(3)	0 ^a	6.0(4)
Ho22	2.6(3)	0	0 ^a	5.4(2)	0	0 ^a	6.0(3)
Ho31	0	0	0 ^a	6.0(2)	4.4(3)	0 ^a	7.5(4)
Ho32	0	0	0 ^a	7.5(2)	0	0 ^a	7.5(2)

$R_F^{\text{nucl}}(\text{obs}) = 2.8\%$, $R_F^{\text{mag}}(\text{obs}) = 4.6\%$, GOF = 1.3

^aManually fixed.

The isotropy subgroup describing such a distortion of high temperature antiferromagnetic structure can be found using ISODISTORT [53]. Superposition of the $m\Gamma_6[k_C]$ irrep responsible for the in-plane spontaneous magnetization and $m\Delta_6[k_{IC}]$ irrep responsible for the incommensurate magnetic structure just below the Néel temperature $T_N \approx 32$ K has been considered. It was found that superposing the in-plane ferromagnetic contribution from $m\Gamma_6$ to the incommensurate structure associated with $m\Delta_6(a, a, b)$ further lowers the MSSG from $Cmc2_1.1'(00g)0sss$ to either $Cmc'2'_1(00g)000$ or $Cm'c2'_1(00g)s0s$, in which both have index $i = 2$ relative to $Cmc2_1.1'(00g)0sss$ (see Table II). We were not able to determine which one of the two models better describes the neutron diffraction data at $T = 4.5$ K because no convergence was reached on the Rietveld refinement of both models when 33 magnetic parameters ascribed to 5 magnetically nonequivalent Ho sites and two harmonics of \mathbf{k}_{IC} were adjusted.

D. Thermal expansion of Ho₇Rh₃

The thermal expansion rate $\Delta l/l_0$ and the coefficient of linear thermal expansion (CTE) α plotted as functions of temperature are shown in Fig. 10(a). As one can see, thermal expansion rate $\Delta l(T)/l_0$ exhibits nonmonotonic behavior revealing negative thermal expansion below 60 K and a shallow minimum centered in the low temperature range at $T_{\min} = 40.5$ K. Cooling the sample below T_{\min} , one can observe a magnetovolume anomaly smeared over a wide temperature range $\Delta T \approx 30$ K below and above the Néel temperature. It should be noted that the sharp magnetovolume anomaly associated with the first-order magnetostructural phase transition

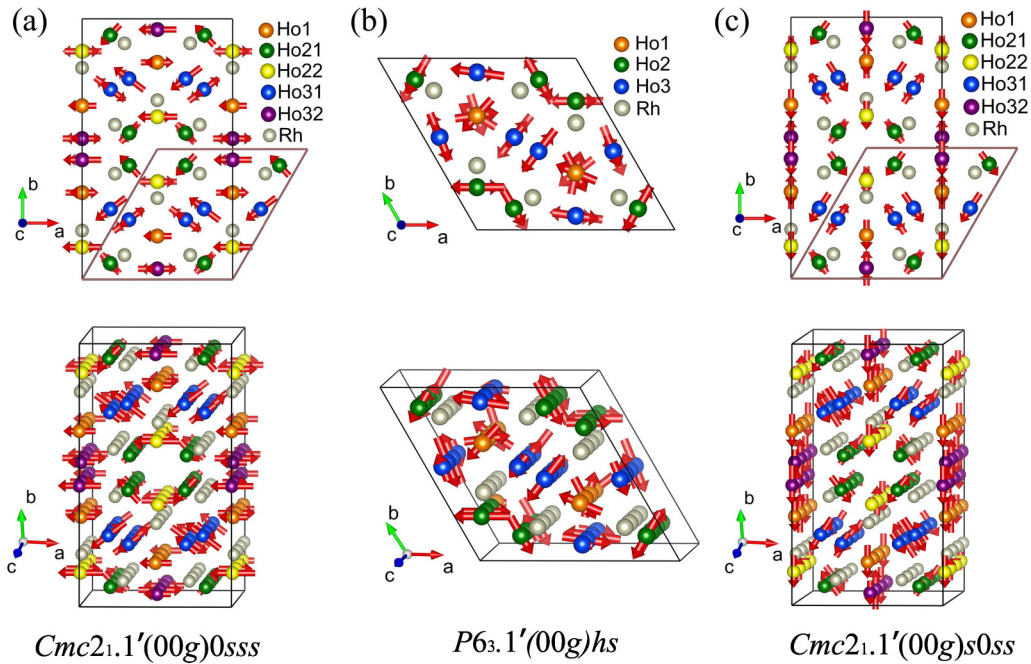


FIG. 8. Schematic visualisation of the refined magnetic structures of Ho_7Rh_3 obtained using the model of MSSG (a) $Cmc2_1.1'(00g)0sss$, (b) $P6_3.1'(00g)hs$ and (c) $Cmc2_1.1'(00g)s0ss$ as projected on the basal plane and as a 3D model. Both parent hexagonal cell and supercell are shown for the basal plane projections.

from antiferromagnetic to ferromagnetic state was previously observed in the isostructural Nd_7Pd_3 compound [25]. The synchrotron diffraction revealed lowering of the symmetry from $P6_3mc$ to $Cmc2_1$ in this compound. In order to check if the crystal structure phase transition affects the thermal expansion of Ho_7Rh_3 in the low temperature range, we performed synchrotron x-ray diffraction in a wide temperature range below and above the Néel temperature. No visible sign of the phase transition towards lower symmetry structure was found on the x-ray diffraction data of Ho_7Rh_3 [see Fig. 10(b)]. Particularly, a comparison of the x-ray diffraction data taken at 8, 28, and 50 K in the q range where one may expect orthorhombic splitting of the Bragg peaks is shown in the inset of Fig. 10(b).

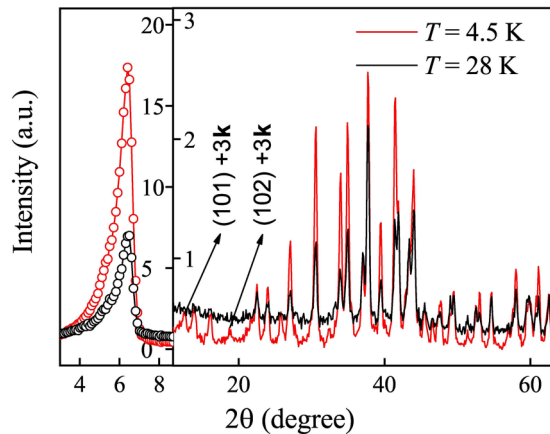


FIG. 9. Neutron powder diffraction patterns for Ho_7Rh_3 measured at $T = 28$ and 4.8 K.

E. Discussion

Three magnetic phase transitions were observed in Ho_7Rh_3 on cooling: (i) transition from paramagnetic to incommensurate SDW structure at $T_N = 32$ K, (ii) squaring-up process developing in the SDW structure below $T_1 \approx 22$ K, and (iii) emergence of ferromagnetic component in the incommensurate magnetic structure below $T_2 \approx 9$ K. Magnetic structure just below the Néel temperature $T_N = 32$ K was described by the propagation vector $\mathbf{k}_{\text{IC}} = (000.389)$ and magnetic superspace group $Cmc2_1.1'(00g)0sss$ associated with the single $m\Delta_6$ irrep. Contrary, it has been suggested in Refs. [24,25] that combination of both $m\Delta_5$ and $m\Delta_6$ is necessary for a proper fit of the zeroth satellite $(000m)$. Our analysis of the extinction rules for MSSGs associated with the $m\Delta_5$ irrep revealed that any model of magnetic structure described by this irrep does not contribute to the zeroth satellite $(000m)$. We have shown that single irrep $m\Delta_6$ is well enough to fit the $(000m)$ magnetic Bragg peak in Ho_7Rh_3 . Moreover, every particular magnetic superspace group associated with the $m\Delta_6$ irrep based on a two-dimensional small irrep restricts the form of a magnetic modulation in a unique way [see Figs. 8(a)–8(c)] while no such restrictions can be provided by the traditional representation analysis. Thus the magnetic superspace groups approach turns out to be a particularly effective tool for analysis of magnetic structure of $R_7\text{Rh}_3$ compounds.

Gignoux *et al.* [54] questioned the stability of the amplitude modulated magnetic structures in rare-earth intermetallic compounds exhibiting strong easy-axis anisotropy. It was found that such magnetic structures could not persist at low temperatures due to entropy considerations and revealed a tendency to evolve towards equal momentum structures via

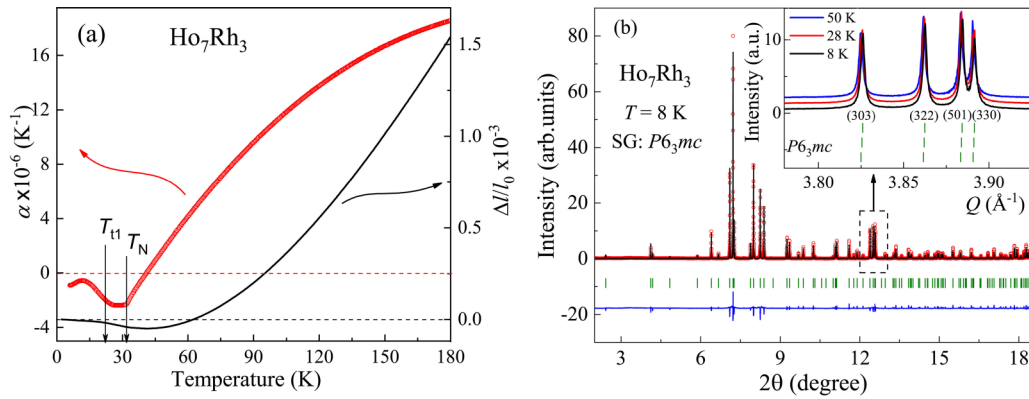


FIG. 10. (a) The temperature dependence of the thermal expansion rate $\Delta l/l_0$ of Ho_7Rh_3 (black line) and calculated linear coefficient of the thermal expansion α (red symbols). (b) Le-Bail fit of the synchrotron diffraction data at $T = 8 \text{ K}$ by the model of the hexagonal $P6_3mc$ structure. The inset displays a comparison of part of the x-ray diffraction patterns measured at 8, 28, and 50 K (see the text).

lock-in transition or squaring-up process. This is exactly what we observe on cooling in the easy-plane Ho_7Rh_3 compound below $T_{T1} \approx 22 \text{ K}$. Small jumps on the AC and DC magnetic measurements data as well as emergence of the Bragg peaks associated with the third harmonic $3k_{TC}$ evidence a squaring-up process in TSW structure of Ho_7Rh_3 . The squaring-up process in applied magnetic field seems to break a full antiferromagnetic compensation and gives rise to a small in-plane ferromagnetic component below T_{T1} which was observed in magnetic measurements data reported for the single crystal sample [14].

Further cooling of Ho_7Rh_3 reveals one more magnetic phase transition associated with large anomalies of both AC and DC magnetic susceptibilities at $T_{T2} \approx 9 \text{ K}$. This transition is accompanied by a nonlinearity in magnetic response to the oscillating magnetic field below 9 K as evidenced by $\chi''_{1\omega}(T)$, $\chi'_{2\omega}(T)$, and $\chi'_{3\omega}(T)$ curves. In particular, a peak of the second harmonic $\chi'_{2\omega}(T)$ at $T_{T2} \approx 9 \text{ K}$ implies that time-inversion symmetry is broken and the ferromagnetic component of the magnetic structure emerges. In terms of magnetic superspace groups formalism, this means lowering of symmetry from the AFM superspace group $Cmc2_1.1'(00g)0sss$ to one of the subgroups of index $i = 2$ $Cmc'2'_1(00g)000$ or $Cm'c2'_1(00g)s0s$ which are compatible with the in-plane ferromagnetic component observed on the single crystal sample [14]. Contrary, the $P6_3.1'(00g)hs$ group revealing good description of the experimental data at $T = 28 \text{ K}$ does not have the magnetic subgroups compatible with the in-plane ferromagnetism. It means that a proper model of the high temperature magnetic structure should be $Cmc2_1.1'(00g)0sss$ despite the good fit quality of the neutron diffraction pattern at $T = 28 \text{ K}$ provided by a model of $P6_3.1'(00g)hs$ group. Thus, the $P6_3.1'(00g)hs$ model reported by us for high temperature incommensurate magnetic structure in Ho_7Rh_3 [55] is incorrect despite the very good fit quality. We also have to emphasize that the nonlinear AC-magnetic susceptibility can be considered as a source of direct and complementary data about breaking of time-inversion or spatial symmetry in magnetic materials helping to analyze magnetic structures with the magnetic superspace groups approach.

As soon as spontaneous magnetization emerges below 9 K, the material decomposes into magnetic domains in order to

minimize its magnetostatic energy. The magnetic measurements data previously reported for the single crystal Ho_7Rh_3 evidenced a large magnetic anisotropy between c axis and basal plane giving rise to narrow domain walls having the size of a few interatomic distances [14]. Magnetic properties of highly anisotropic ferromagnets and ferrimagnets with narrow domain walls are known to be substantially affected by domain walls movement, pinning and freezing effects [56,57]. Particularly, slowing of magnetic dynamics and time-dependent effects on the AC magnetic susceptibility data, which are typical for spin-glass-like systems, were reported for numerous ferromagnetic or ferrimagnetic materials with narrow domain walls [42,43,58–60]. Thus observation of glasslike effects on the AC magnetic susceptibility data below 9 K can be ascribed to the domain walls movement and pinning effects. A small external DC magnetic field of $H_{DC} \approx 200 \text{ Oe}$ was found to push the sample to the one-domain state eliminating glasslike effects from the AC magnetic susceptibility data.

The presence of the short-range antiferromagnetic order directly observed in Ho_7Rh_3 by neutron diffraction and deviation of the inverse susceptibility from the CW law could explain anomalous behavior of the thermal expansion in a wide temperature range $T_N < T < 2T_N$. Magnetoelastic interactions along with the strong magnetocrystalline anisotropy affect the lattice well above the Néel temperature. Moreover, the short-range antiferromagnetic correlations seems to be a driving force of the anomalous behavior of electrical resistivity previously reported for Ho_7Rh_3 and other members of $R_7\text{Rh}_3$ family above the Néel temperature in Refs. [14,37]. It should be noted that enhanced short-range antiferromagnetic correlations persisting up to high temperatures were reported to substantially affect magnetic, thermal and electrical properties of different members of R_3T [9,61–63] and $R_5\text{Pd}_2$ [40,64] families. Enhanced short-range magnetic order persisting up to high temperatures was explained in terms of a model of indirect exchange interaction introduced by Campbell [65] for pure rare-earth metals. This model suggests that an intra-atomic $4f$ - $5d$ exchange followed by an interatomic $5d$ - $5d$ hybridization between neighboring R atoms leads to a $4f$ - $5d$ - $5d$ - $4f$ exchange interaction. When it comes to R -rich binary rare-earth intermetallic compounds

of $R_n T_m$ type, this exchange interaction is accompanied by a $4f-5d-3d(4d)-5d-4f$ exchange giving rise to a competition of two types of RKKY exchange interactions. Close examination of the Ho₇Rh₃ crystal structure reveals that the shortest Ho1-Ho3 distance is 3.485 Å, the shortest Ho2-Ho2 distance is 3.341 Å, and the shortest Ho3-Ho3 distance is 3.617 Å while in pure Ho metal the minimal Ho-Ho distance is 3.486 Å. The shortest distance between two Rh atoms engaged in the neighboring trigonal prisms is 4.381 Å. Thus indirect $4f-5d-5d-4f$ exchange apparently dominates over the Ho-Ho network in the crystal structure of Ho₇Rh₃ and may give rise to the short-range magnetic order persisting well above the Néel temperature.

IV. CONCLUSION

In this work, DC and AC magnetic measurements, heat capacity, thermal expansion, as well as neutron and synchrotron powder diffraction were performed in order to study crystal structure and low temperature magnetic states in Ho₇Rh₃. We found that incommensurate magnetic structure described with the magnetic superspace group $Cmc2_1.1'(00g)0sss$ and propagation vector $\mathbf{k}_{IC} = (000.389)$ emerges just below the Néel temperature $T_N = 32$ K. A spin-reorientation transition at $T_{r1} \approx 22$ K was ascribed to development of the squaring-up

process while the ferromagnetic component emerges in the incommensurate magnetic structure below $T_{r2} \approx 9$ K. Short-range antiferromagnetic order observed in a wide temperature range in the nominally paramagnetic state was found to affect thermal expansion and seems to be a driving force of the anomalous behavior of electrical resistivity above the Néel temperature. No symmetry lowering of the hexagonal crystal structure was observed by synchrotron diffraction in a wide temperature range below and above the Néel temperature. Finally, we showed that nonlinear AC-magnetic susceptibility measurements could be a source of direct data about symmetry breaking effects in magnetic material which benefits to a symmetry analysis of complex magnetic structures and magnetic phase transitions.

ACKNOWLEDGMENTS

The authors acknowledge Dr. A. Fitch and European Synchrotron Radiation Facility for access to the ID22 station, experiment HC-4364. This work was partly supported by the Ministry of Science and Higher Education of the Russian Federation (Project No. 122021000031-8 and 122021000034-9) and Russian Foundation for Basic Research (Project No. 20-32-90047). K.S. thanks Russian Science Foundation Grant No. 22-22-20033.

-
- [1] M. Smidman, M. B. Salamon, H. Q. Yuan, and D. F. Agterberg, *Rep. Prog. Phys.* **80**, 036501 (2017).
 - [2] S. Mühlbauer, B. Binz, F. Jonietz, C. Pfleiderer, A. Rosch, A. Neubauer, R. Georgii, and P. Böni, *Science* **323**, 915 (2009).
 - [3] S. Okumura, S. Hayami, Y. Kato, and Y. Motome, *Phys. Rev. B* **101**, 144416 (2020).
 - [4] R. B. Roof Jr, A. C. Larson, and D. T. Cromer, *Acta Cryst.* **14**, 1084 (1961).
 - [5] G. Olcese, *J. Less-Common Met.* **33**, 71 (1973).
 - [6] J. Moreau and E. Parthé, *J. Less-Common Met.* **32**, 91 (1973).
 - [7] E. Parthé and J.-M. Moreau, *J. Less-Common Met.* **53**, 1 (1977).
 - [8] K. Taylor, *Adv. Phys.* **20**, 551 (1971).
 - [9] N. Baranov, A. Proshkin, A. Gubkin, A. Cervellino, H. Michor, G. Hilscher, E. Gerasimov, G. Ehlers, M. Frontzek, and A. Podlesnyak, *J. Magn. Magn. Mater.* **324**, 1907 (2012).
 - [10] K. Sengupta and E. V. Sampathkumaran, *Phys. Rev. B* **73**, 020406(R) (2006).
 - [11] K. Sengupta, S. Rayaprol, and E. V. Sampathkumaran, *J. Phys.: Condens. Matter* **16**, L495 (2004).
 - [12] T. Tsubotaoka, Y. Nishiume, T. Tokunaga, Y. Nakamori, Y. Andoh, S. Kawano, G. Nakamoto, and M. Kurisu, *Phys. B: Condens. Matter* **327**, 352 (2003).
 - [13] T. Tsubotaoka, T. Matsushita, A. V. Proshkin, E. G. Gerasimov, P. B. Terentev, and N. V. Baranov, *J. Alloys Compd.* **628**, 230 (2015).
 - [14] T. Tsubotaoka, K. Obata, A. A. Sherstobitov, E. Gerasimov, P. Terentev, and N. Baranov, *J. Alloys Compd.* **654**, 126 (2016).
 - [15] Y. J. Wang, Y. S. Du, Y. Q. Zhang, L. Li, J. Q. Deng, L. Ma, J. Wang, and G. H. Rao, *J. Alloys Compd.* **847**, 156379 (2020).
 - [16] N. K. Singh, P. Kumar, Z. Mao, D. Paudyal, V. Neu, K. G. Suresh, V. K. Pecharsky, and K. A. G. Jr, *J. Phys.: Condens. Matter* **21**, 456004 (2009).
 - [17] M. Klimczak, E. Talik, R. Troć, K. Gofryk, and D. Badurski, *J. Alloys Compd.* **442**, 172 (2007).
 - [18] F. Canepa, M. Napolitano, and S. Cirafici, *Intermetallics* **10**, 731 (2002).
 - [19] K. Umeo, Y. Echizen, M. H. Jung, T. Takabatake, T. Sakakibara, T. Terashima, C. Terakura, C. Pfleiderer, M. Uhlarz, and H. v. Löhneysen, *Phys. Rev. B* **67**, 144408 (2003).
 - [20] S. Iikubo, S. Yoshii, T. Kageyama, K. Oda, Y. Kondo, K. Murata, and M. Sato, *J. Phys. Soc. Jpn.* **70**, 212 (2001).
 - [21] X. Xu, S. Kawano, T. Tsubotaoka, H. Fukuda, T. Tokunaga, Y. Andoh, M. Kurisu, and G. Nakamoto, *Phys. B: Condens. Matter* **241-243**, 742 (1997).
 - [22] T. Tsubotaoka, Y. Andoh, S. Kawano, G. Nakamoto, D. T. K. Anh, M. Kurisu, and T. Tokunaga, *J. Alloys Compd.* **408-412**, 181 (2006).
 - [23] H. Kadowaki, K. Motoya, T. Kawasaki, T. Osakabe, H. Okumura, K. Kakurai, K. Umeo, and T. Takabatake, *J. Phys. Soc. Jpn.* **69**, 2269 (2000).
 - [24] S. Rayaprol, V. Siruguri, A. Hoser, C. Ritter, and E. V. Sampathkumaran, *Phys. Rev. B* **90**, 134417 (2014).
 - [25] Y. Mudryk, C. Ritter, D. Paudyal, A. Provino, S. K. Dhar, P. Manfrinetti, F. Fauth, and V. K. Pecharsky, *J. Phys.: Condens. Matter* **31**, 265801 (2019).
 - [26] J. M. Perez-Mato, J. L. Ribeiro, V. Petricek, and M. I. Aroyo, *J. Phys.: Condens. Matter* **24**, 163201 (2012).
 - [27] V. Petříček, J. Fuksa, and M. Dusek, *Acta Cryst. A* **66**, 649 (2010).
 - [28] M. Mito, K. Iriguchi, H. Deguchi, J.-i. Kishine, K. Kikuchi, H. Ohsumi, Y. Yoshida, and K. Inoue, *Phys. Rev. B* **79**, 012406 (2009).
 - [29] M. Suzuki, *Prog. Theor. Phys.* **58**, 1151 (1977).
 - [30] S. Fujiki and S. Katsura, *Prog. Theor. Phys.* **65**, 1130 (1981).

- [31] T. Shirane, T. Moriya, T. Bitoh, A. Sawada, H. Aida, and S. Chikazawa, *J. Phys. Soc. Jpn.* **64**, 951 (1995).
- [32] E. M. Clements, R. Das, M.-H. Phan, L. Li, V. Keppens, D. Mandrus, M. Osofsky, and H. Srikanth, *Phys. Rev. B* **97**, 214438 (2018).
- [33] R. K uchler, A. W orl, P. Gegenwart, M. Berben, B. Bryant, and S. Wiedmann, *Rev. Sci. Instrum.* **88**, 083903 (2017).
- [34] V. Petř ıcek, M. Duřek, and L. Palatinus, *Z. Kristallogr.- Crystal. Mater.* **229**, 345 (2014).
- [35] B. J. Campbell, H. T. Stokes, D. E. Tanner, and D. M. Hatch, *J. Appl. Cryst.* **39**, 607 (2006).
- [36] B. J. Campbell, H. T. Stokes, J. M. Perez-Mato, and J. Rodr ıguez-Carvajal, *Acta Cryst. A* **78**, 99 (2022).
- [37] T. Tsutaoka, Y. Nakamori, T. Tokunaga, and Y. Itoh, *J. Phys. Soc. Jpn.* **70**, 199 (2001).
- [38] K. Binder and A. P. Young, *Rev. Mod. Phys.* **58**, 801 (1986).
- [39] J. A. Mydosh, *Spin Glasses: An Experimental Introduction* (Taylor and Francis, London, 1993).
- [40] A. F. Gubkin, E. A. Sherstobitova, P. B. Terentyev, A. Hoser, and N. V. Baranov, *J. Phys.: Condens. Matter* **25**, 236003 (2013).
- [41] J. L. Dormann, L. Bessais, and D. Fiorani, *J. Phys. C* **21**, 2015 (1988).
- [42] V. Tsurkan, J. Hemberger, M. Klemm, S. Klimm, A. Loidl, S. Horn, and R. Tidecks, *J. Appl. Phys.* **90**, 4639 (2001).
- [43] Y. G. Pastushenkov, K. P. Skokov, E. S. Antonova, T. I. Ivanova, and J. S. Bartolom e, *J. Alloys Compd.* **689**, 894 (2016).
- [44] Y. Bitla and S. N. Kaul, *Europhys. Lett.* **96**, 37012 (2011).
- [45] A. V. Lazuta, I. I. Larionov, and V. A. Ryzhov, *J. Exp. Theor. Phys.* **73**, 1086 (1991).
- [46] N. Narita and I. Yamada, *J. Phys. Soc. Jpn.* **65**, 4054 (1996).
- [47] S. Chikazumi, *Physics of Ferromagnetism* (Oxford University Press, New York, 1997).
- [48] A. P. Cracknell, B. Davies, S. C. Miller, and W. F. Love, *Kronecker Product Tables. Volume 1. General Introduction and Tables of Irreducible Representation of Space Groups* (IFI/Plenum, New York, 1979).
- [49] S. van Smaalen, B. J. Campbell, and H. T. Stokes, *Acta Cryst. A* **69**, 75 (2013).
- [50] H. T. Stokes and B. J. Campbell, *Acta Cryst. A* **78**, 364 (2022).
- [51] S. V. Gallego, E. S. Tasci, G. de la Flor, J. M. Perez-Mato, and M. I. Aroyo, *J. Appl. Cryst.* **45**, 1236 (2012).
- [52] J. Perez-Mato, S. Gallego, E. Tasci, L. Elcoro, G. de la Flor, and M. Aroyo, *Annu. Rev. Mater. Res.* **45**, 217 (2015).
- [53] H. T. Stokes and B. J. Campbell, *Acta Cryst. A* **73**, 4 (2017).
- [54] D. Gignoux and D. Schmitt, *J. Magn. Magn. Mater.* **129**, 53 (1994).
- [55] A. F. Gubkin, A. A. Vaulin, T. Tsutaoka, and N. V. Baranov, *Phys. Met. Metallogr.* **120**, 1152 (2019).
- [56] N. V. Baranov, A. F. Gubkin, A. P. Vokhmyanin, A. N. Pirogov, A. Podlesnyak, L. Keller, N. V. Mushnikov, and M. I. Bartashevich, *J. Phys.: Condens. Matter* **19**, 326213 (2007).
- [57] D. Gignoux and R. Lemaire, *Solid State Commun.* **14**, 877 (1974).
- [58] H. Mamiya and S. Nimori, *J. Phys.: Condens. Matter* **24**, 336006 (2012).
- [59] M. Bałanda, in *Relaxation Phenomena. Liquid Crystals, Magnetic Systems, Polymers, High-Tc Superconductors, Metallic Glasses*, edited by W. Haase and S. Wr obel (Springer, Berlin, 2003), p. 96.
- [60] M. Bałanda, *Acta Phys. Pol. A* **124**, 964 (2013).
- [61] A. F. Gubkin, L. S. Wu, S. E. Nikitin, A. V. Suslov, A. Podlesnyak, O. Prokhnenko, K. Prokeř, F. Yokaichiya, L. Keller, and N. V. Baranov, *Phys. Rev. B* **97**, 134425 (2018).
- [62] A. Herrero, A. Oleaga, A. Gubkin, A. Salazar, and N. Baranov, *J. Alloys Compd.* **808**, 151720 (2019).
- [63] A. Herrero, A. Oleaga, A. Gubkin, M. Frontzek, A. Salazar, and N. Baranov, *Intermetallics* **111**, 106519 (2019).
- [64] A. Vaulin, A. Chirkova, E. Sherstobitova, D. Shishkin, E. Sherokalova, K. Skokov, N. Baranov, and A. Gubkin, *Intermetallics* **144**, 107519 (2022).
- [65] I. A. Campbell, *J. Phys. F* **2**, L47 (1972).